COMBINING GROUND PENETRATING RADAR WITH TERRESTRIAL LiDAR SCANNING TO OBSERVE THE SPATIAL DISTRIBUTION OF LIQUID WATER CONTENT IN SEASONAL SNOWPACKS

Ryan Webb[1], Noah Molotch[1], and Michael Fend[2]

ABSTRACT

An important consideration for water resource planning is snowmelt runoff timing. Runoff timing can be determined by the difficult to observe physical process of water movement through a seasonal snowpack. The aim of this study is to present a novel method that combines light detection and ranging (LiDAR) with ground penetrating radar (GPR) to non-destructively observe the spatial distribution of bulk liquid water content in a seasonal snowpack during spring snowmelt. We develop these methods in a manner to be applicable within a short time window, making it possible to spatially observe rapid changes that occur to this property (sub-daily timescale). We applied these methods at three experimental plots across elevational gradients in Colorado, showing the high variability of liquid water content in snow. Volumetric liquid water contents ranged from near zero to 19% within the scale of meters. We also show the rapid changes in bulk liquid water content that occur over sub-daily time scales. Results of this study show the importance of the lateral flow of water in higher elevation snowpacks and how this process may change in a future climate. The presented methods have a reasonable amount of uncertainty in bulk liquid water content (maximum of 1.5%) making this an applicable method for future studies to observe the complex spatio-temporal dynamics of liquid water in snow. (KEYWORDS: snowmelt, flowpaths, liquid water in snow, dye tracers, GPR, LiDAR)

INTRODUCTION

Appropriately representing snowmelt infiltration is important to predicting streamflow (McNamara et al., 2005). However, snowmelt infiltration is highly variable temporally (Webb et al., 2017) and spatially as a result of preferential flowpaths that form in a snowpack (Avanzi et al., 2017; Schneebeli, 1995; Webb et al., 2015; Williams et al., 2010). The flow of water down sloping interfaces creates localized infiltration (Webb et al., 2018a,b) and can deposit water directly into a stream channel, bypassing soil interaction (Eiriksson et al., 2013). One-dimensional (vertical) water flow modeling through snow has improved runoff estimates in flat, open terrain (Avanzi et al., 2016; Wever et al., 2014; Würzer et al., 2017). However, the complexity of this process increases as slope and forest canopy effects are introduced (Webb et al., 2018a), justifying the need to observe the spatial variability of meltwater flow in complex environments to properly constrain modeling efforts.

Several methods exist to remotely monitor changes to the cryosphere over large areas (Cao et al., 2015; Flanner et al., 2011; Pistone et al., 2014; Richardson et al., 2014; Tedesco et al., 2013) but complications arise in complex terrain, forested areas, or when the snow becomes wet. Airborne measurements have improved current techniques for observing complex individual headwater catchments (Bair et al., 2016; Painter et al., 2016). However, these methods are unable to capture rapid changes in properties such as liquid water content (LWC) due to limited temporal resolution. Continuously observing the LWC of snow has also advanced in recent years for point measurements using upward looking ground penetrating radar (GPR) (Heilig et al., 2015; Schmid et al., 2015). Spatially observing LWC has been accomplished over short distances (Bradford et al., 2009; Techel and Pielmeier, 2011). However, measuring the LWC of snow currently requires destructive sampling methods; e.g. when using instruments like a Denoth Meter or Finnish Snow Fork (e.g. Techel and Pielmeier, 2011). The use of GPR has recently afforded non-destructive sampling of LWC in snow. For example, Bradford et al. (2009) non-destructively observed LWC over a 35 m long transect using 16 passes over the same transect. These above methods for observing the LWC of snow are limited either spatially to a point or temporally to a single point in time.

Paper presented Western Snow Conference 2018
[1] Ryan Webb, Campus Box 450, INSTAAR, University of Colorado, Boulder, CO, 80309-0450, ryan.w.webb@colorado.edu
[1] Noah Molotch, Campus Box 450, INSTAAR, University of Colorado, Boulder, CO, 80309-0450, noah.molotch@colorado.edu
[2] Michael Fend, UNAVCO, Boulder, CO, fend@unavco.org

Two methods that have yet to be combined are light detection and ranging (LiDAR) and GPR. LiDAR has been extensively used to map snow depth in complex terrain (Deems et al., 2013; Deems et al., 2008; Painter et al., 2016) and GPR has been used effectively to survey snow for almost any environmental condition (Holbrook et al., 2016; Marshall and Koh, 2008; Marshall et al., 2007; Webb, 2017). However, these two well established methods have yet to be combined to fully exploit the benefits of each. For this study, we combine the spatial distribution of snow depth using a terrestrial LiDAR system with measurements of dielectric properties of the snowpack from a common offset pulse wave GPR system. To our knowledge, this is the first time these types of datasets have been combined to non-destructively derive the spatial distribution of LWC in a melting snowpack.

The goal of this study is to present a novel methodology that combines LiDAR and GPR to non-destructively observe the spatial distribution of bulk LWC in a seasonal snowpack during spring snowmelt. We aim to develop these methods to be applicable in a short time window, making it possible to observe rapid changes (i.e. sub-daily timescales) that occur to these properties spatially.

MATERIALS AND METHODS

Field Sites

The developed methods were tested at two locations in the Niwot Ridge research area in the Colorado Rocky Mountains, one near treeline (NT) at an elevation of 3350 masl and one above treeline (AT) at an elevation of 3530 masl. Each site has continuous observations of snow depth and air temperature adjacent to experimental plots. Both sites have southern facing slope aspects and ~10° slope angles. The NT site is an open meadow that develops a large, prominent snow drift from westward winds and bounding forest whereas the AT is a leeward hillslope that receives wind deposition across the entire site. The experimental plots are approximately 800 m^2 for NT and 1100 m^2 for AT with ~200 m of GPR surveys conducted at each location. Snowmelt was surveyed at NT on April 12, 2017 and at AT twice on May 15 and once on May 16, 2017 to observe changes in LWC at the sub-daily and daily timescales.

Terrestrial LiDAR

The spatial distribution of snow depth (d_s) was determined using the well-established method of terrestrial LiDAR scanning (Deems et al., 2013; Painter et al., 2016). We used a Riegl VZ-400 LiDAR scanner from a single scan position for each study site. Georeferencing and aligning multiple scans was accomplished using Riegl RiSCAN Pro software. Ground surface scans occurred in September, 2016 and were georeferenced using four 16.5 cm diameter reflective targets with Trimble R10 rover GPS units (minimum of 20 minute occupation time) corrected to a Trimble NetR9 base station with a Zephyr Geodetic antenna. During these scans, at least 5 additional 5-cm diameter reflective discs were attached to permanent structures (e.g. buildings, scaffolding, etc.) and large tree trunks as permanent tie points. Snow surface scans occurred in the spring of 2017 from as close to the original scan position as possible. Permanent tie points and planar structures were used to align all scans through the RiSCAN multi-scan adjustment processing. The accuracy of these methods was determined to be 2 cm or less. The LiDAR scans were aggregated to produce 50 cm resolution digital elevation models (DEMs) of the ground and snow surfaces. Snow depth was then calculated by subtracting the ground surface DEMs from snow surface DEMs.

Ground Penetrating Radar

Two-way-traveltime (TWT) of GPR waves through snow were obtained on the same days as snow surface LiDAR scans. We used a Mala Geoscience, Inc. ProEx control unit pulse GPR system with an 800 MHz shielded antenna. The antenna was fixed in place on a plastic sled towed behind the user (Figure 1). A GPS antenna connected to the ProEx control unit registered location information every second. Survey transects were marked with 2.5 cm diameter, 30 cm long plastic pipes inserted halfway into the snow every five to ten meters along the transect. Fiducial marks were created at these markers for alignment of all surveys. Both the survey ski tracks and the markers were discernable in LiDAR scans, allowing for quality assessment of alignment.

Radar pulses were triggered on 0.05 s intervals using eight times stacking and a total time window of 50 ns. The average survey travel speed was ~0.5 m/s resulting in ~40 returns per meter. The RadExplorer Software package (Deco-Geophysical Co ltd., distributed by Mala Geosciences) was used for time-zero adjustment, taken as the first break in the first wavelet, a dewow filter, and spherical divergence correction to compensate for signal attenuation. The reflection of the snow-soil interface (e.g. Figure 1) was then picked and TWT averaged over 50 cm increments.

(a)

(b)

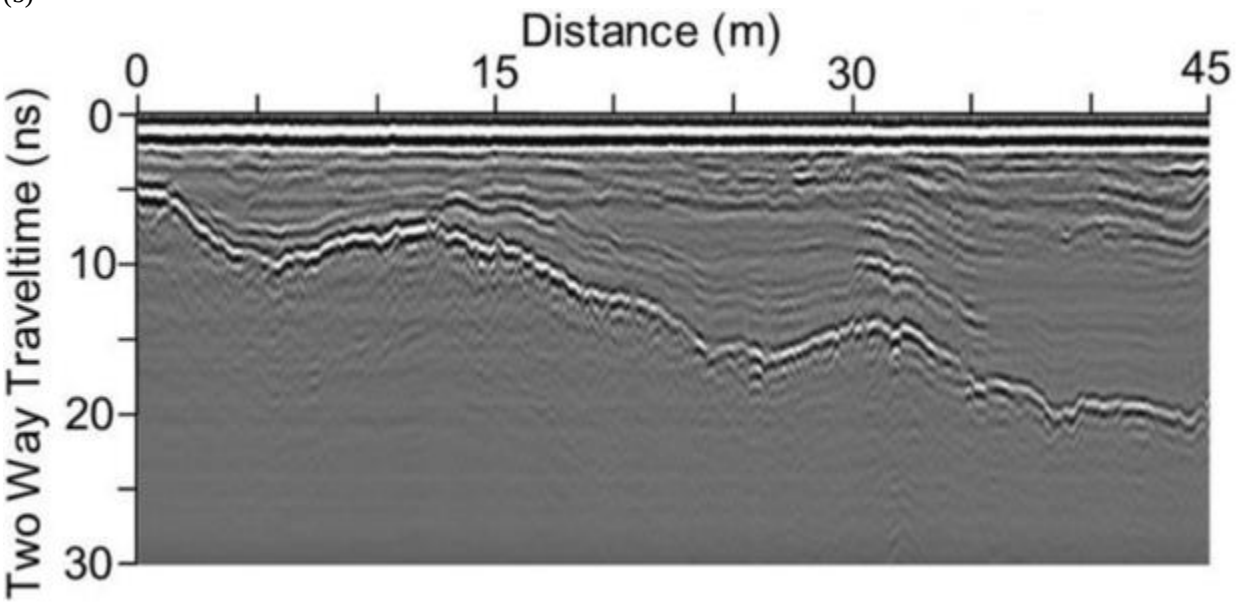

Figure 1. (a) The ground penetrating radar unit being towed behind the user (left) and (b) an example radargram clearly showing the reflection from the snow-soil interface (right).

Liquid Water Content Inversion

A GPR pulse is an electromagnetic wave that travels through the snowpack and is reflected off changes in material properties such as density, with the strongest reflection often from the snow-soil interface (Figure 1) (Bradford et al., 2009; Holbrook et al., 2016; Webb, 2017). The effective dielectric permittivity (ε_{eff}) of snow is

sensitive to snowpack density and LWC (Bradford et al., 2009; Heilig et al., 2015), and is calculated from the observed velocity (v) of the radar wave through (e.g. Mitterer et al., 2011):

$$\varepsilon_{eff} = \left(\frac{v}{c}\right)^2 \quad \text{(Eq. 1)}$$

Where c is the speed of light in a vacuum (~0.3 m/ns) and v is calculated using:

$$v = \frac{d_s}{\left({}^{TWT}/_{2}\right)} \quad \text{(Eq. 2)}$$

The bulk volumetric LWC (θ_w) of snow is calculated from ε_{eff} using the Roth et al. (1990) three phase mixing model that is commonly applied (Heilig et al., 2015; Koch et al., 2014; Mitterer et al., 2011; Schmid et al., 2015):

$$\theta_w = \frac{\varepsilon_{eff}^{0.5} - \frac{\rho_d}{\rho_i}\varepsilon_i^{0.5} - \left(1 - \frac{\rho_d}{\rho_i}\right)\varepsilon_a^{0.5}}{\varepsilon_w^{0.5} - \varepsilon_a^{0.5}} \quad \text{(Eq. 3)}$$

Where ρ_d is the dry density of snow, ρ_i is the density of ice (917 kg/m3), ε_i, ε_a, and ε_w are the dielectric permittivities of ice, air, and liquid water, respectively. At 0° C these dielectric permittivities are known (ε_i = 3.18, ε_a = 1.0, and ε_w = 87.9). For this study we observe ρ_d through manual snow pit measurements and assume it is spatially uniform within each plot.

Manual Snow Observations

Manual snow pit observations were collected adjacent to experimental plots on the same day of surveys. Density profiles were collected at 10 cm increments using a 1 L wedge cutter, grain size and type were observed with a hand lense and crystal card, and temperatures measured using dial thermometers at 10 cm increments. The bulk density (ρ_s) from snow pit profiles were taken as the average of all 1 L density measurements. The ρ_d parameter for equation (3) was estimated from ρ_s using:

$$\rho_s = \rho_d + \theta_w \rho_w \quad \text{(Eq. 4)}$$

Where ρ_w is the density of liquid water. We estimate a weighted average θ_w for each 10 cm density from visually observed wetness (dry = 0.00, moist = 0.02, wet = 0.06, very wet = 0.12, and slushy = 0.15) to estimate ρ_d from ρ_s (Bradford et al., 2009; Techel and Pielmeier, 2011). This qualitative estimation introduces minimal error at the observed density values (> 300 kg/m3) when using equation (3) due to the low sensitivity of calculations to density (Figure 2).

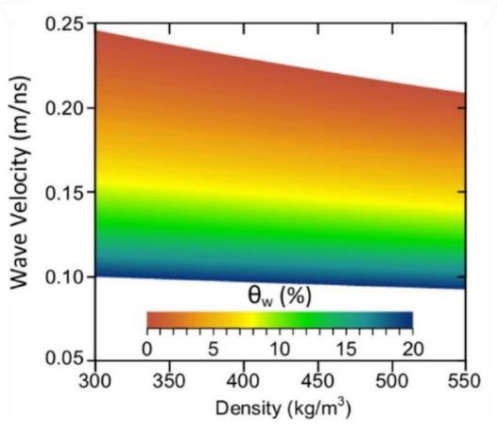

Figure 2. The results of liquid water content using equation (3) for a range of densities between 300 and 550 kg/m3 and the observed velocity of the radar wave.

RESULTS

Each snow survey captured snowpacks approaching isothermal conditions with observed surface melt. Meteorological conditions during the AT survey were highly variable due to an approaching storm. The average ρ_s was 438 kg/m^3 for NT and 472 kg/m^3 for AT corresponding to estimated ρ_d values of 425 kg/m^3 (~3% LWC) and 450 kg/m^3 (~5% LWC), respectively.

The snow-soil interface resulted in strong GPR reflections over the entire length of each transect (example for NT shown in Figure 1). Observed radar velocities ranged from 0.1 m/ns to 0.23 m/ns at NT, and 0.13 m/ns to 0.24 m/ns at AT. Resulting θ_w ranged from 0 to 19% for NT and 0 to 10% for AT. The NT site shows large differences of 13% θ_w over a distance of only 1 m (Figure 3). The NT site showed these large differences over short distances multiple times at areas where LWC appear to accumulate (Figure 4). The AT observations had slightly less variability with changes of nearly 9% over a similar distance (Figure 5). Average θ_w was 3.4% for NT and 1.6%, 2.7%, and 2.4% for AT on May 15 at ~1 pm, May 15 ~3 pm, and May 16 ~7 pm, respectively (Figure 5).

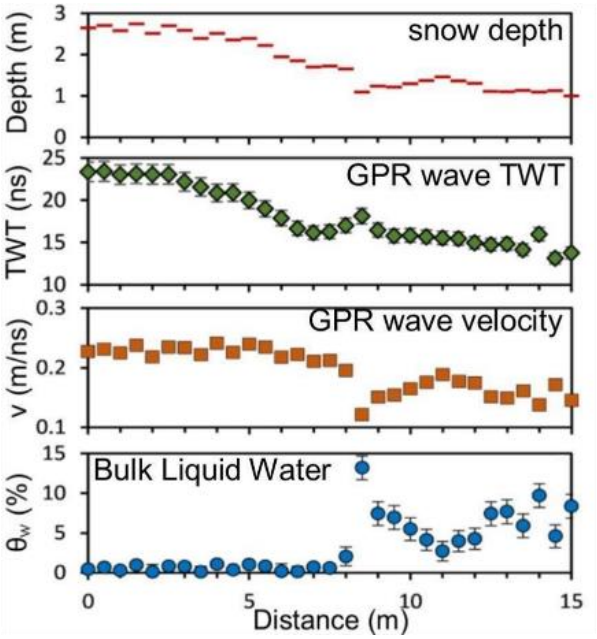

Figure 3. Example results at the near tree line site along a 15 m section displaying the observed snow depth, GPR travel time, calculated velocity, and bulk liquid water content.

The AT surveys show rapid increase in θ_w over a 2 hour period with multiple locations increasing by 5% (Figure 5). The total range change was -2 to 5% displaying the high spatial variability, though most of the plot increased from 0 to 5% (Figure 5). At the daily timescale, changes varied from -4 to 5% over a 30 h period. Patterns of high and low θ_w at AT occurred at similar locations for all three surveys (Figure 5).

The NT d_s distribution shows the prominent snow drift that forms each year (Figure 4). This produced large incidence angles from the LiDAR scan position combined with poor reflectance due to a wet snow surface in some areas, reducing the area successfully surveyed for d_s (blank areas in Figure 4). The AT site produced less LiDAR issues providing successful d_s observations for the entire plot (Figure 5). The range of observed d_s was 0.1 m to 2.8 m for NT and 0.6 m to 2.8 m for AT.

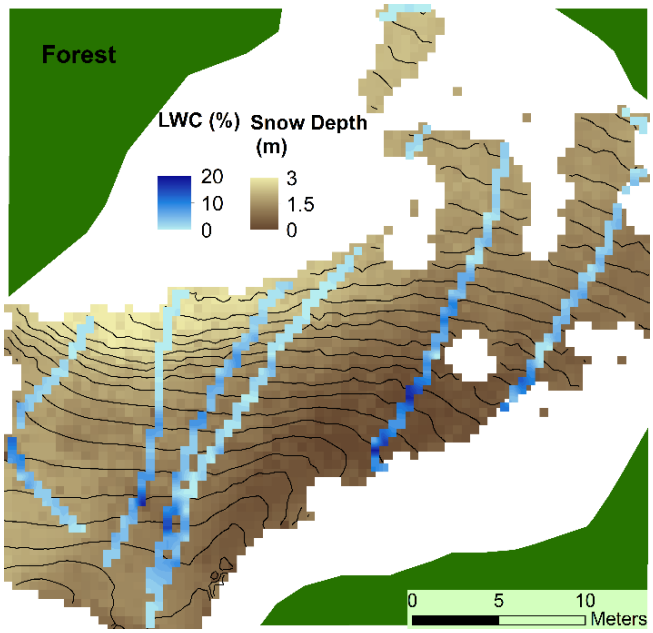

Figure 4. Results of the near treeline survey showing the spatial distribution of snow depth and bulk liquid water content. Contours shown are snow surface elevation at 0.25 m intervals.

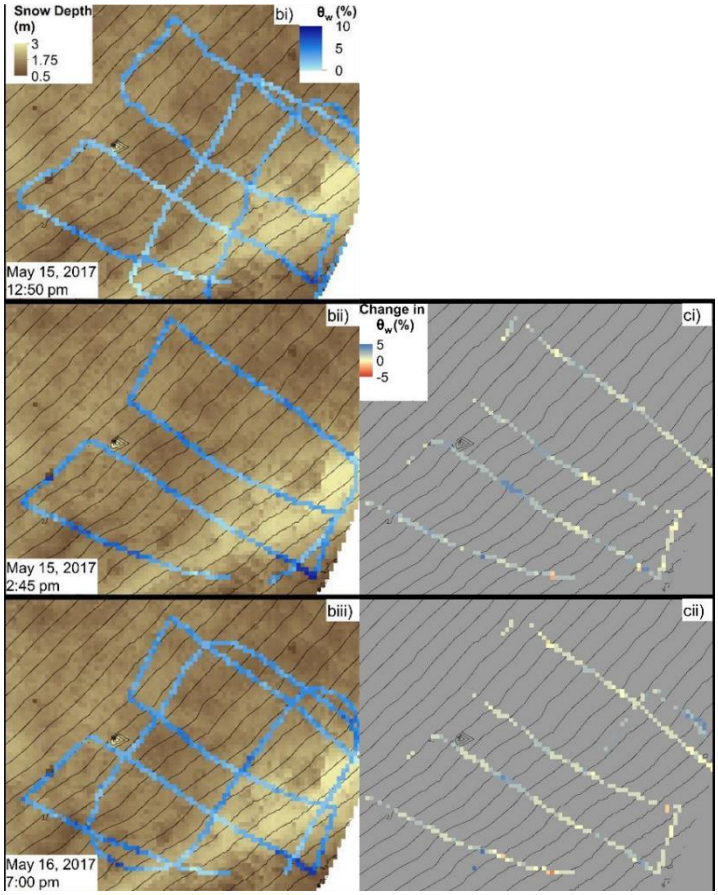

Figure 5. Results of the above treeline surveys showing the spatial distribution of snow depth and bulk liquid water contents for three different surveys (left) and the change in bulk liquid water content between surveys (right). Contours shown are snow surface elevation at 0.25 m intervals.

DISCUSSION

We were successful in non-destructively observing the spatial distribution of θ_w in a melting snowpack at spatial scales not previously achieved. The shortest time between surveys was two hours, though this method could be applied at sub-hourly time steps. The 200 m transects were surveyed within ten minutes, thus 1000 m transects could potentially be surveyed at hourly time steps. The LiDAR scans were more time-limiting, taking approximately 30 minutes at the single scan position. However, the GPR and LiDAR data presented in this study were collected by an individual investigator during snowmelt and the total survey time could be shortened with multiple investigators that independently collect GPR, LiDAR, and snow pit observations.

This study shows the high spatio-temporal variability in θ_w that can only be observed in a non-destructive manner. Though snow depth can be measured using a depth probe, this would destroy the microstructure and layer interfaces at each probe location, creating vertical pathways for the draining of liquid water from a snowpack. The non-destructive methods of LiDAR allow for the movement of liquid water within a snowpack to occur undisturbed.

Uncertainty in Methods

Unrealistic θ_w values occurred in less than 5% of all observations within the range of uncertainty (slightly negative, generally > -0.5% θ_w). The highest uncertainty occurred at NT in shallow snow depth. The 2 cm snow depth accuracy results in increased uncertainty in θ_w observations for shallow snow through velocity calculations using equation (2). Observed snow depth at NT was as low as 0.1 m. However, average depth along transects was 1.37 m at NT and 2.04 m at AT propagating to an average θ_w uncertainty less than 0.005 from snow depth.

A second source of uncertainty originates in picking the snow-soil interface reflection in GPR data. We estimate a TWT uncertainty less than 5% from the wavelength of the 800 MHz antenna. This propagates to an average θ_w uncertainty less than 0.007 that will increase for low snow depths.

Additional uncertainty occurs in snow density observations and LWC approximations using equation (4). The 1 L wedge cutter is accurate within 5% (Proksch et al., 2016) and we estimate the manual LWC approximations could error up to 5% resulting in a maximum dry snow density uncertainty of 10%. This results in θ_w uncertainty less than 0.002 due to the minimal impact of density on θ_w (Figure 2). The uncertainties discussed above combine for an estimated total θ_w uncertainty of 0.015 (1.5%).

Implications

The results of this study show the large variability in θ_w that occurs over short distances and time periods during melt. This is the first time observations of θ_w in a melting snowpack have been made at these scales. The NT site showed the highest spatial variability with θ_w values up to 19.5% and large differences over distances of 1 m (Figure 3, 4). The AT site showed the high temporal variability with changes in θ_w ranging from -2% to 5% over a 2 hour period displaying rapid non-uniform temporal variability that occurs (Figure 5). Furthermore, the full range of changes in θ_w occur within a space of a few meters (Figure 5). Liquid water within a snowpack is more spatially and temporally variable than previously observed along shorter transects (Bradford et al., 2009; Techel and Pielmeier, 2011).

Both NT and AT show the highest θ_w values in downslope areas of each plot. For NT, high θ_w occurs in similar locations of high snowmelt discharge in snow lysimeters, at the edges of the snow drift (Webb et al., 2018b). For AT we observed the spatial and temporal variability of θ_w, showing changes from -2 to 5% LWC over two hours. Furthermore, the observed θ_w values on the sloping terrain of our study are higher than those in flat terrain (Heilig et al., 2015; Koch et al., 2014; Schmid et al., 2015), offering new insight towards the physical process diverting and storing liquid water in a snowpack at the plot scale.

To observe what layer interfaces were diverting meltwater, a complimentary dye tracer experiment was occurring at the same time as this study. The dye tracers showed a thicker flow path for AT, a thin flow path NT, and no lateral flow paths for an additional experiment in the montane zone (Figure 6). In combination with an energy budget analysis to estimate melt rates for each study plot, we estimate that the AT observed changes in θ_w are a result of flow paths converging from a total contributing area of ~17 m^2. At NT we estimate a total contributing area of ~6 m^2. This combined with the dye tracer experiments suggests that longitudinal flow paths are more

prominent at higher elevations. In a warming climate, higher elevation snowpacks may shift to have similar snow conditions as the lower elevation sites, reducing the influence of lateral intra-snowpack flow paths.

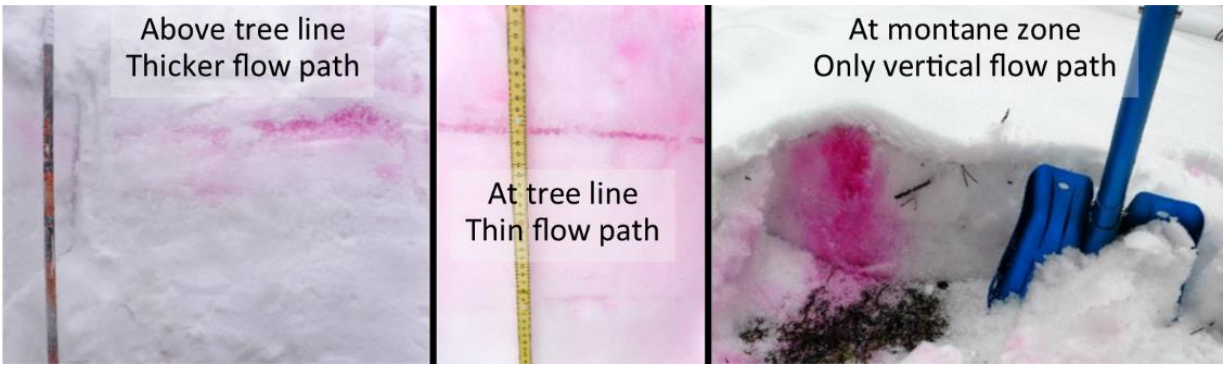

Figure 6. Results of dye tracer experiment showing flow paths that cause longitudinal flow of meltwater.

Water flowing downslope through snow creates localized areas of high θ_w (Figure 4). However, the average θ_w observed are similar to those using upward looking GPR (Heilig et al., 2015; Mitterer et al., 2011; Schmid et al., 2015) and GPS (Koch et al., 2014). Point measurements may capture average θ_w but lack information about the spatial variability of changes. The methods presented here offer insights towards the distance that liquid water moves through a snowpack. At the length scales observed (tens of meters), accumulated meltwater will result in localized basal discharge that may create saturated flowpaths in the shallow subsurface (Webb et al., 2018a) and potentially affect stream-hillslope hydrologic connectivity. The presented methods will be useful for future investigations of these complex processes.

CONCLUSIONS

We were able to non-destructively observe the spatial distribution of liquid water in a melting snowpack at spatial scales and time intervals not previously achieved. This method can be used to observe rapid changes in the bulk liquid water content of a snowpack at the plot and hillslope scales within 1.5% volumetric liquid water content. Results display the high spatial and temporal variability of liquid water content in a seasonal snowpack during melt. Results near treeline displayed observations of 0.6% and 13.2% volumetric liquid water content separated by only 1 m. Results above treeline show changes in liquid water content ranging from -2% to 5% over a 2-hr period and from -4% to 5% over a 30-hr period. This shows the non-uniform manner that a snowpack diverts and stores liquid water. Future investigations will benefit from applying the presented methods to observe the spatial distribution of liquid water content in a snowpack that can vary rapidly. Additional benefit will be gained from utilizing technological advances with ground-based radar observations.

REFERENCES

Avanzi, F., H. Hirashima, S. Yamaguchi, T. Katsushima, and C. De Michele. 2016. Observations of capillary barriers and preferential flow in layered snow during cold laboratory experiments, Cryosphere, 10(5), 2013-2026, doi: 10.5194/tc-10-2013-2016.

Avanzi, F., G. Petrucci, M. Matzl, M. Schneebeli, and C. De Michele. 2017. Early formation of preferential flow in a homogeneous snowpack observed by micro-CT, Water Resources Research, 53(5), 3713-3729, doi: 10.1002/2016WR019502.

Bair, E., K. Rittger, R. Davis, T. Painter, and J. Dozier. 2016. Validating reconstruction of snow water equivalent in California's Sierra Nevada using measurements from the NASA Airborne Snow Observatory, Water Resources Research, 52(11), 8437-8460, doi: 10.1002/2016WR018704.

Bradford, J., J. Harper, and J. Brown. 2009. Complex dielectric permittivity measurements from ground-penetrating radar data to estimate snow liquid water content in the pendular regime, Water Resources Research, 45, doi: 10.1029/2008WR007341.

Cao, Y., S. Liang, X. Chen, and T. He. 2015. Assessment of Sea Ice Albedo Radiative Forcing and Feedback over the Northern Hemisphere from 1982 to 2009 Using Satellite and Reanalysis Data, Journal of Climate, 28(3), 1248-1259, doi: 10.1175/JCLI-D-14-00389.1.

Deems, J., T. Painter, and D. Finnegan. 2013. Lidar measurement of snow depth: a review, Journal of Glaciology, 59(215), 467-479, doi: 10.3189/2013JoG12J154.

Deems, J. S., S. R. Fassnacht, and K. J. Elder. 2008. Interannual Consistency in Fractal Snow Depth Patterns at Two Colorado Mountain Sites, Journal of Hydrometeorology, 9(5), 977-988, doi: 10.1175/2008jhm901.1.

Eiriksson, D., M. Whitson, C. H. Luce, H. P. Marshall, J. Bradford, S. G. Benner, T. Black, H. Hetrick, and J. P. McNamara. 2013. An evaluation of the hydrologic relevance of lateral flow in snow at hillslope and catchment scales, Hydrological Processes, 27(5), 640-654, doi: 10.1002/hyp.9666.

Flanner, M., K. Shell, M. Barlage, D. Perovich, and M. Tschudi. 2011. Radiative forcing and albedo feedback from the Northern Hemisphere cryosphere between 1979 and 2008, Nature Geoscience, 4(3), 151-155, doi: 10.1038/ngeo1062|10.1038/NGEO1062.

Heilig, A., C. Mitterer, L. Schmid, N. Wever, J. Schweizer, H. Marshall, and O. Eisen. 2015. Seasonal and diurnal cycles of liquid water in snow-Measurements and modeling, Journal of Geophysical Research-Earth Surface, 120(10), 2139-2154, doi: 10.1002/2015JF003593.

Holbrook, W., S. Miller, and M. Provart. 2016. Estimating snow water equivalent over long mountain transects using snowmobile-mounted ground-penetrating radar, Geophysics, 81(1), WA183-WA193, doi: 10.1190/GEO2015-0121.1.

Koch, F., M. Prasch, L. Schmid, J. Schweizer, and W. Mauser. 2014. Measuring Snow Liquid Water Content with Low-Cost GPS Receivers, Sensors, 14(11), 20975-20999, doi: 10.3390/s141120975.

Marshall, H., and G. Koh (2008), FMCW radars for snow research, Cold Regions Science and Technology, 52(2), 118-131, doi: 10.1016/j.coldregions.2007.04.008.

Marshall, H., M. Schneebeli, and G. Koh. 2007. Snow stratigraphy measurements with high-frequency FMCW radar: Comparison with snow micro-penetrometer, Cold Regions Science and Technology, 47(1-2), 108-117, doi: 10.1016/j.coldregions.2006.08.008.

McNamara, J. P., D. Chandler, M. Seyfried, and S. Achet. 2005. Soil moisture states, lateral flow, and streamflow generation in a semi-arid, snowmelt-driven catchment, Hydrological Processes, 19(20), 4023-4038, doi: 10.1002/hyp.5869.

Mitterer, C., A. Heilig, J. Schweizer, and O. Eisen. 2011. Upward-looking ground-penetrating radar for measuring wet-snow properties, Cold Regions Science and Technology, 69(2-3), 129-138, doi: 10.1016/j.coldregions.2011.06.003.

Painter, T., et al. 2016. The Airborne Snow Observatory: Fusion of scanning lidar, imaging spectrometer, and physically-based modeling for mapping snow water equivalent and snow albedo, Remote Sensing of Environment, 184, 139-152, doi: 10.1016/j.rse.2016.06.018.

Pistone, K., I. Eisenman, and V. Ramanathan. 2014. Observational determination of albedo decrease caused by vanishing Arctic sea ice, Proceedings of the National Academy of Sciences of the United States of America, 111(9), 3322-3326, doi: 10.1073/pnas.1318201111.

Proksch, M., N. Rutter, C. Fierz, and M. Schneebeli. 2016. Intercomparison of snow density measurements: bias, precision, and vertical resolution, Cryosphere, 10(1), 371-384, doi: 10.5194/tc-10-371-2016.

Richardson, M., I. Davenport, and R. Gurney. 2014. Global Snow Mass Measurements and the Effect of Stratigraphic Detail on Inversion of Microwave Brightness Temperatures, Surveys in Geophysics, 35(3), 785-812, doi: 10.1007/s10712-013-9263-x.

Roth, K., R. Schulin, H. Fluhler, and W. Attinger. 1990. Calibration of Time Domain Reflectometry for Water-Content Measurement using a Composite Dielectric Approach, Water Resources Research, 26(10), 2267-2273, doi: 10.1029/WR026i010p02267.

Schmid, L., F. Koch, A. Heilig, M. Prasch, O. Eisen, W. Mauser, and J. Schweizer. 2015. A novel sensor combination (upGPR-GPS) to continuously and nondestructively derive snow cover properties, Geophysical Research Letters, 42(9), 3397-3405, doi: 10.1002/2015GL063732.

Schneebeli, M. 1995. Development and stability of preferential flow paths in a layered snowpack, paper presented at Biogeochemistry of Seasonally Snow-Covered Catchments, IAHS, Boulder, CO.

Techel, F., and C. Pielmeier. 2011. Point observations of liquid water content in wet snow - investigating methodical, spatial and temporal aspects, The Cryosphere, 5(2), 405-418, doi: 10.5194/tc-5-405-2011.

Tedesco, M., X. Fettweis, T. Mote, J. Wahr, P. Alexander, J. Box, and B. Wouters. 2013. Evidence and analysis of 2012 Greenland records from spaceborne observations, a regional climate model and reanalysis data, Cryosphere, 7(2), 615-630, doi: 10.5194/tc-7-615-2013.

Webb, R. 2017. Using ground penetrating radar to assess the variability of snow water equivalent and melt in a mixed canopy forest, Northern Colorado, Frontiers of Earth Science, 11(3), 482-495, doi: 10.1007/s11707-017-0645-0.

Webb, R., S. Fassnacht, and M. Gooseff. 2017a. Defining the Diurnal Pattern of Snowmelt using a Beta Distribution Function, Journal of the American Water Resources Association, 53(3), 684-696, doi: 10.1111/1752-1688.12522.

Webb, R. W., S. R. Fassnacht, and M. N. Gooseff. 2015. Wetting and Drying Variability of the Shallow Subsurface Beneath a Snowpack in California's Southern Sierra Nevada, Vadose Zone Journal, 14(8), 0, doi: 10.2136/vzj2014.12.0182.

Webb, R. W., S. R. Fassnacht, and M. N. Gooseff. 2018a. Hydrologic Flowpath Development Varies by Aspect during Spring Snowmelt in Complex Subalpine Terrain, The Cryosphere, 2017, 1-24, doi: 10.5194/tc-2017-12.

Webb, R. W., M. Williams, and T. Erickson. 2018. The Spatial and Temporal Variability of Meltwater Flowpaths: Insights from a grid of over 100 Snow Lysimeters, Water Resources Research.

Wever, N., C. Fierz, C. Mitterer, H. Hirashima, and M. Lehning. 2014. Solving Richards Equation for snow improves snowpack meltwater runoff estimations in detailed multi-layer snowpack model, Cryosphere, 8(1), 257-274, doi: 10.5194/tc-8-257-2014.

Williams, M. W., T. A. Erickson, and J. L. Petrzelka. 2010. Visualizing meltwater flow through snow at the centimetre-to-metre scale using a snow guillotine, Hydrological Processes, doi: 10.1002/hyp.7630.

Würzer, S., N. Wever, R. Juras, M. Lehning, and T. Jonas. 2017. Modelling liquid water transport in snow under rain-on-snow conditions - considering preferential flow, Hydrology and Earth System Sciences, 21(3), 1741-1756, doi: 10.5194/hess-21-1741-2017.